



Stable hybrid perovskite $\text{MAPb}(\text{I}_{1-x}\text{Br}_x)_3$ for photocatalytic hydrogen evolution



Zhijie Zhao^a, Jiaojiao Wu^a, Yan-Zhen Zheng^{b,*,*}, Nan Li^a, Xitao Li^a, Zhili Ye^a, Siyu Lu^{c,*,*}, Xia Tao^{a,b,*}, Chuncheng Chen^d

^a State Key Laboratory of Organic-Inorganic Composites, Beijing University of Chemical Technology, 15 Beisanhuan East Road, Beijing 100029, PR China

^b Research Center of the Ministry of Education for High Gravity Engineering & Technology, Beijing University of Chemical Technology, 15 Beisanhuan East Road, Beijing 100029, PR China

^c College of Chemistry and Molecular Engineering, Zhengzhou University, Zhengzhou 450000, PR China

^d Key Laboratory of Photochemistry, Beijing National Laboratory for Molecular Sciences Institute of Chemistry, University of Chinese Academy of Sciences, PR China

ARTICLE INFO

Keywords:

$\text{MAPb}(\text{I}_{1-x}\text{Br}_x)_3$
Hydrogen evolution
Perovskite
Photocatalyst
Visible light

ABSTRACT

Hybrid organic-inorganic perovskites have been pursuing for solar/visible-driven H_2 evolution from hydrohalic acid (HX) splitting, but their inherent structural stability and performance are still challenging. Herein, we report on a stable hybrid perovskite $\text{MAPb}(\text{I}_{1-x}\text{Br}_x)_3$ ($x = 0\text{--}0.20$) obtained by one-pot crystallization in a mixed halide parent solution and its implementation as a newcomer photocatalyst for H_2 evolution in aqueous HX solution. $\text{MAPb}(\text{I}_{1-x}\text{Br}_x)_3$ is demonstrated to be a superior visible-light-driven photocatalyst for H_2 evolution in aqueous HI/HBr solution with no Pt as a cocatalyst. An optimized $\text{MAPb}(\text{I}_{1-x}\text{Br}_x)_3$ ($x = 0.10$) shows a highest H_2 evolution rate of $1471 \mu\text{mol h}^{-1} \text{g}^{-1}$ under visible light ($\lambda \geq 420 \text{ nm}$) illumination, which is ~40 times higher than that of pure MAPbI_3 , and the dual-halide perovskite is rather stable showing no obvious decrease in the photocatalytic activity over 60 runs (252 h). The perovskite inherent structural stability is further evidenced by XRD, UV-vis spectra and EDS elemental mapping of $\text{MAPb}(\text{I}_{1-x}\text{Br}_x)_3$ measured after cycled photocatalytic reaction. The solar HI splitting efficiency of $\text{MAPb}(\text{I}_{1-x}\text{Br}_x)_3$ ($x = 0.10$) is determined as 1.42%. The mechanism behind photocatalytic H_2 evolution enhancement is elucidated by the experimental and computational methods.

1. Introduction

Organic-inorganic hybrid lead halogen perovskites have attracted considerable interest as photoabsorbers for solar energy conversion due to their unique optoelectronic properties [1–5]. The lead halogen perovskites have the general formula APbX_3 , where A is an organic cation and X is a halogen ion. Methylammonium lead iodine (MAPbI_3), the most attractive and representative perovskite, has been widely applied into photovoltaic devices [6–8], and also being investigated for photoelectrochemical hydrogen evolution [9–11], light-emitting diodes [12,13], lasers [14,15], and photo-detectors [16]. Recently, MAPbI_3 has shown to be effective in photocatalytic H_2 evolution by splitting hydrohalic acids [9]. Photocatalytic hydrohalic acids splitting, as a potential alternative process to water splitting, exhibits low overpotential [17,18], high theoretical solar-to-hydrogen efficiency [19] and valuable by-products such as I_2/I_3^- [20]. Several pioneering works mainly focus

on constructing composites of MAPbI_3 with TiO_2/Pt or reduced graphene oxide to promote the photogenerated electron transportation and subsequently photocatalytic H_2 evolution reaction (HER) rate [21,22]. It has been demonstrated that the mixed halides $\text{MAPb}(\text{I}_{1-x}\text{X}_x)_3$ with X representing Br, or Cl possess the prolonged charge carrier life and enlarged bandgap with adjustable conduction band potential compared to the parent MAPbI_3 , which has been evidenced in perovskite-based solar cells [23]. Most recently, Huang et al. reported I-doped MAPbBr_3 with a bandgap funnel structure via a light-assisted halide method, resulting in accelerated charge carriers and enhanced HER activity [24]. Indeed, partial substitution of iodine ion (I^- , 2.20 \AA) with a relatively smaller radius bromine (Br^- , 1.96 \AA) endows the perovskite material more merits including stable cubic structure against ambient moisture and/or oxygen [25], effective charge transportation [26] as well as relatively broad absorption region [27]. Thus, we herein imagine if there is any other possibility of achieving high-performance,

* Corresponding author at: State Key Laboratory of Organic-Inorganic Composites, Beijing University of Chemical Technology, 15 Beisanhuan East Road, Beijing 100029, PR China.

** Corresponding authors.

E-mail addresses: zhengyz@mail.buct.edu.cn (Y.-Z. Zheng), sylu2013@zzu.edu.cn (S. Lu), taoxia@mail.buct.edu.cn (X. Tao).

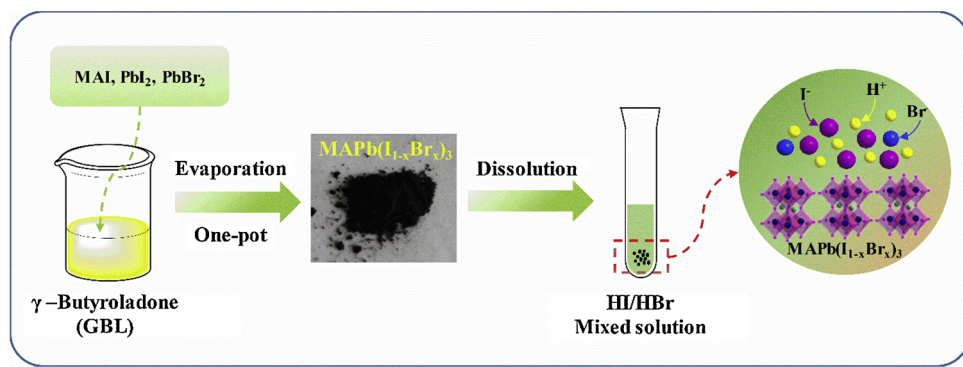


Fig. 1. Schematic diagram of $\text{MAPb}(\text{I}_{1-x}\text{Br}_x)_3$ crystal formation process.

stable perovskite photocatalyst for H_2 evolution by incorporating Br anion in the MAPbI_3 crystal matrix, which is unexplored yet an engaging topic.

In this work, we prepare a series of dual-halide perovskites i.e. $\text{MAPb}(\text{I}_{1-x}\text{Br}_x)_3$ ($x = 0\text{--}0.20$) by simultaneous codeposition of MAI, PbI_2 , and PbBr_2 from thermostatically controlled heating device, in which Br/I ratios are tuned by increasing the deposition rate of PbBr_2 with respect to PbI_2 while keeping the rate of MAI constant. The preparation procedure for $\text{MAPb}(\text{I}_{1-x}\text{Br}_x)_3$ crystals can be found in Fig. 1. We find that $\text{MAPb}(\text{I}_{1-x}\text{Br}_x)_3$ powder can effectively split HI into H_2 under visible light irradiation ($\lambda \geq 420 \text{ nm}$) without Pt cocatalyst. $\text{MAPb}(\text{I}_{1-x}\text{Br}_x)_3$ ($x = 0.10$) achieves the highest visible-light-driven photocatalytic HER rate of $1471 \mu\text{mol h}^{-1} \text{g}^{-1}$, far higher than that of MAPbI_3 ($37 \mu\text{mol h}^{-1} \text{g}^{-1}$). Furthermore, $\text{MAPb}(\text{I}_{1-x}\text{Br}_x)_3$ ($x = 0.10$) shows no obvious decrease in the photocatalytic activity after 252 h. This is the first exploration on one-pot-synthesized stable hybrid perovskite $\text{MAPb}(\text{I}_{1-x}\text{Br}_x)_3$ photocatalyst for H_2 evolution in aqueous HX solution.

2. Experimental section

2.1. Materials synthesis

The $\text{MAPb}(\text{I}_{1-x}\text{Br}_x)_3$ photocatalyst was synthesized as shown in Fig. 1. To get the dual-halide perovskite powders, a series of $\text{MAPb}(\text{I}_{1-x}\text{Br}_x)_3$ ($x = 0, 0.05, 0.10, 0.15, 0.20$) precursor solutions were prepared firstly. The precursor solutions were prepared by mixing PbI_2 , PbBr_2 and MAI according to the expectant ratio in Gamma-butyrolactone (GBL) at 60°C . For instance, $\text{MAPb}(\text{I}_{1-x}\text{Br}_x)_3$ ($x = 0.10$) was prepared by dissolving 0.9 mmol PbI_2 , 0.1 mmol PbBr_2 and 1 mmol MAI in 4 mL of GBL. Similarly, $\text{MAPb}(\text{I}_{1-x}\text{Br}_x)_3$ ($x = 0\text{--}0.20$) precursor solutions were synthesized through the same procedure except for the different ratios of PbI_2 and PbBr_2 used. The solution was heated to 100°C and held overnight to grow the crystals. The $\text{MAPb}(\text{I}_{1-x}\text{Br}_x)_3$ precipitates were centrifuged with diethyl ether to remove residual solvent, then the obtained powders were finally dried in a vacuum oven at 60°C overnight.

2.2. Preparation of HI/HBr mixed saturated solution and stability map experiment

Firstly, 1 g of MAPbI_3 powder was added to 2 mL of aqueous HI solution, and then sonicated and shaken for 30 min to reach dynamic equilibrium for MAPbI_3 saturated HI solution. MAPbBr_3 saturated HBr solution was prepared using a method similar to the MAPbI_3 saturated HI solution synthesis, except that HBr was used instead of HI. After that, a series of mixed solutions were prepared by mixing the supernatant liquid from two saturated solution according to default mole ratio of I and Br. Stability map of $\text{MAPb}(\text{I}_{1-x}\text{Br}_x)_3$ ($x = 0.05, 0.10, 0.15, 0.20$) under different mixed solution was performed. Firstly, 200 mg of $\text{MAPb}(\text{I}_{1-x}\text{Br}_x)_3$ powder was added to 1 mL of every prepared mixed solution and sonicated for 5 min . Then, the solution with the powder was shaken for 30 min for stabilization. The $\text{MAPb}(\text{I}_{1-x}\text{Br}_x)_3$ precipitates were centrifuged respectively with ethyl acetate and diethyl ether to remove residual solvent, then the obtained powders were finally dried in a vacuum oven at 60°C overnight. The stability of $\text{MAPb}(\text{I}_{1-x}\text{Br}_x)_3$ powder was verified by X-ray diffraction (XRD) pattern measurement.

$(\text{I}_{1-x}\text{Br}_x)_3$ powder was added to 1 mL of every prepared mixed solution and sonicated for 5 min . Then, the solution with the powder was shaken for 30 min for stabilization. The $\text{MAPb}(\text{I}_{1-x}\text{Br}_x)_3$ precipitates were centrifuged respectively with ethyl acetate and diethyl ether to remove residual solvent, then the obtained powders were finally dried in a vacuum oven at 60°C overnight. The stability of $\text{MAPb}(\text{I}_{1-x}\text{Br}_x)_3$ powder was verified by X-ray diffraction (XRD) pattern measurement.

2.3. Characterizations

The crystalline structure of samples was characterized by powder XRD using Cu $\text{K}\alpha$ radiation ($\lambda = 0.15406 \text{ nm}$) on a Rigaku D/max-2500 VB2+/PC. X-ray photoelectron spectroscopy (XPS) and valence-band XPS (VB-XPS) of samples were performed on a thermos ESCALAB250 XPS system using an Al $\text{K}\alpha$ X-ray source. To compensate for surface charge effects, binding energies were calibrated using the C1s hydrocarbon peak at 284.8 eV . Sample morphologies were observed by scanning electron microscopy (SEM) images on a Hitachi S-4700 microscope. High resolution transmission electron microscopy (HRTEM) images of the synthesized products were carried out on a Hitachi H-9500 microscope. The optical absorption property of samples was determined by using the absorption spectrum performed on a UV-vis spectrophotometer (Perkin Elmer Lambda 950 UV-vis). Photoluminescence (PL) emission and time-resolved spectra were obtained on a Spectrofluorometer FS5 (EDINBURGH INSTRUMENTS) with an excitation wavelength of 347 nm at room temperature.

2.4. Photocatalytic H_2 evolution

The photocatalytic performance of $\text{MAPb}(\text{I}_{1-x}\text{Br}_x)_3$ was assessed using H_2 production experiments under a visible light irradiation ($\lambda \geq 420 \text{ nm}$) of a 300 mW/cm^2 Xe lamp (Beijing China Education Auto-Light Technology Co., Ltd, CEL-HXF300). 20 mg of $\text{MAPb}(\text{I}_{1-x}\text{Br}_x)_3$ powder was dispersed in 10 mL saturated HI/HBr mixed solution (H_3PO_2 , as a selective reducing agent for by-product I_3^- , mixed in a 1:4 volume ratio). Before irradiation, the suspension was thoroughly degassed to remove air by bubbling N_2 for 30 min . The evolved H_2 was analyzed by a gas chromatography (7890 B GC System, Agilent Technologies) with high-purity nitrogen carrier gas. The solar HI splitting efficiency of $\text{MAPb}(\text{I}_{1-x}\text{Br}_x)_3$ ($x = 0.10$) in the mixed acid solution ($\text{HI}/\text{HBr} = 8.25:1.75$ in mole) without H_3PO_2 was measured by Xe lamp with a 420 nm cutoff filter to perform the H_2 generation experiment. The average intensity of irradiation was controlled by changing the distance between the reactor and the photosource to keep on 100 mW/cm^2 . The light intensity was measured using a thermopile sensor (International Light Technologies, ILT 1400-A). The exposed area to light was controlled to be $0.5 \text{ cm} \times 0.5 \text{ cm}$. The standard hydrogen reduction potential was 0 V (versus RHE), and the I^- oxidation potential to I_3^- was 0.53 V (versus RHE). The concentration of HI in the mixed acid solution was 6.25 mol L^{-1} , and the I_3^- ion concentration in

the reduced HI solution was 1.44×10^{-3} mol L⁻¹. Thus, the concentration of H⁺ was calculated to be 7.78 mol L⁻¹, and the redox potential could be determined from the Nernst equation. The solar HI splitting efficiency was calculated using the following equation [9]:

$$\begin{aligned} E(2H+2e^- \rightarrow H_2) &= 0 - 0.059/2 \times \log(1/7.78^2) \\ &= 0.053 \text{ (versus NHE)} \end{aligned} \quad (1)$$

$$\begin{aligned} E(3I^- \rightarrow I_3^- + 2e^-) &= 0.53 + 0.059/2 \times \log(1.44 \times 10^{-3}/6.25^3) \\ &= 0.376 \text{ (versus NHE)} \end{aligned} \quad (2)$$

For this reason, the total potential for the mixed acid solution splitting could be calculated as 0.376 V – 0.053 V = 0.323 V. By using this potential, the solar HI splitting efficiency could be estimated from the following equation:

$$\begin{aligned} \text{Solar HI splitting efficiency (\%)} \\ = \frac{\text{Evolved } H_2 \text{ (mol)} \times 6.02 \times 10^{23} \times 2 \times 0.323 \text{ (eV)} \times 1.6 \times 10^{-19}}{P_{\text{sol}} \text{ (Wcm}^{-2}\text{)} \times \text{Area (cm}^2\text{)} \times \text{time (s)}} \times 100 \end{aligned} \quad (3)$$

2.5. Photoelectrochemical measurements

The photoelectrodes were prepared using plasma-treated fluoridtin oxide (FTO) as substrates. Specifically, the FTO substrates were cleaned with deionized water, absolute ethanol and isopropyl alcohol, respectively, and treated under UV-ozone for 30 min. After that, the desired solution of MAPb(I_{1-x}Br_x)₃ was prepared by dissolution of PbI₂, PbBr₂ and MAI stoichiometrically in 100 μL of GBL. The MAPb(I_{1-x}Br_x)₃ solution was dropped on FTO substrate and then annealed at 100 °C for 20 min under N₂ atmosphere to form the photoelectrodes. The photoelectrochemical properties were investigated in a three-electrode quartz cell with 5 mL saturated HI/HBr mixed solution (H₃PO₂, as a stabilizer, mixed in a 1:4 volume ratio), in which a platinum wire, a saturated calomel electrode and the as-prepared photocatalyst film on FTO substrate were used as the counter, the reference and the working electrode, respectively. A 300 W Xe lamp equipped with a 420 nm cut-off filter was adopted as a light source for the photoelectrochemical experiment. The on-off light photoresponse measurement was performed at the open-circuit potential. Electrochemical impedance spectroscopy (EIS) was measured at a bias voltage of 0 V with the frequency range ranging from 0.1 to 10⁵ Hz.

2.6. Computational methods

We constructed a 2 × 2 supercell of the (010) surface of orthorhombic MAPbI₃ perovskite. To understand the Br defect, one of I atoms on the surface was randomly replaced with a Br atom. A 20 Å vacuum is set up above the slab for pristine and Br-substituted case. All calculations were performed using Vienna ab Initio Simulation Package (VASP) code [28–31], employing projector-augmented wave (PAW) and plane wave basis set for C, N, H, and Pb atoms with a cut-off energy of 600 eV [32]. The PBE exchange functional with the Grimme's DFT-D3 van der Waals dispersion corrections was applied [33]. In each geometry optimization, the MA⁺ ions in the bottom layers are fixed.

3. Results and discussion

3.1. Structures and compositions of photocatalysts

XRD measurement was used to investigate the crystal structure of MAPb(I_{1-x}Br_x)₃ (x = 0–0.20) crystals. As shown in Fig. 2a, the pattern of MAPbI₃ shows several characteristic diffraction peaks at 14.1, 28.1, 28.4, 31.8, 40.4 and 43.0°, corresponding to the (110), (004), (220), (310), (224) and (314) planes, respectively [26]. With the concentration of Br fraction increases, all the XRD peaks shift to larger diffraction

angles, indicating the successful incorporation of Br into MAPbI₃ and consequently demonstrate the formation of MAPb(I_{1-x}Br_x)₃ compound [34]. Furthermore, from the magnified XRD patterns in the region of $2\theta = 27.5\text{--}30.0^\circ$ (Fig. 2b), one can see that upon increasing x from 0 to 0.20, the peak diffracted by the (004) plane gradually disappears and finally merges into a single peak corresponding to (220) plane. This is mainly attributed to the smaller ionic radii of the incorporated Br (1.96 Å) compared with I (2.20 Å) [25]. The HRTEM image in Fig. 2c shows the interplanar distance fringe separation of 0.312 nm, corresponding to the (220) plane of MAPb(I_{1-x}Br_x)₃ (x = 0.10) crystal [35]. EDS mapping of MAPb(I_{1-x}Br_x)₃ (x = 0.10) (Fig. 2d) present a uniform distribution of Pb, Br and I on the perovskite particles. XPS was employed to further probe the surface compositions and electronic structure of MAPb(I_{1-x}Br_x)₃ (x = 0.10) crystal (Fig. 3a–c). The XPS full scan spectrum demonstrates the existence of C, N, I, Br and Pb elements on the surface. The elemental analysis manifests that the Br content of MAPb(I_{1-x}Br_x)₃ (x = 0.10) crystal surface is estimated as 10.6%, analogous to the initial amount added in the preparation process.

3.2. Dynamic equilibrium of photocatalysts in solution

Considering that MAPb(I_{1-x}Br_x)₃ is a water-soluble ionic compound and stable in saturated aqueous solutions similar to other conventional ionic crystals, the dynamic equilibrium of the dissolution and precipitation of MAPb(I_{1-x}Br_x)₃ in HI/HBr mixed aqueous solution system should be explored herein. Specifically, In order to obtain a stable MAPb(I_{1-x}Br_x)₃ suspension (x = 0.10, for example), as-prepared MAPb(I_{1-x}Br_x)₃ (x = 0.10) powder are first transferred into the HI/HBr mixed solution with the mole ratio of 9.00/1.00 until ionic crystals started to precipitate. The obtained precipitates after dipping (denoted as MAPb(I_{1-n}Br_n)₃) were characterized by XRD. By XRD measurement (Fig. S1), it is found that all peak positions of MAPb(I_{1-n}Br_n)₃ shift towards small angles in comparison with pristine sample MAPb(I_{1-x}Br_x)₃, indicating the Br content in the perovskite matrix decrease (i.e. n < x) [36]. Thus, to guarantee the MAPb(I_{1-x}Br_x)₃ (x = 0.10) composition in the suspension, other three HI/HBr mixed solutions with the mole Br ratios i.e. 8.50/1.50, 8.25/1.75 and 8.00/2.00 are also prepared in parallel. By virtue of the XRD results (see Fig. S1), it is found that when the mole ratio of HI/HBr is 8.00/2.00, all peak positions of MAPb(I_{1-n}Br_n)₃ comparing with MAPb(I_{1-x}Br_x)₃ shift to larger diffraction angles, which means the ratio of HBr in the mixed solution is excessive, resulting in that the Br content of MAPb(I_{1-n}Br_n)₃ is higher than that of MAPb(I_{1-x}Br_x)₃ (i.e. n > x). However, all peak positions of MAPb(I_{1-x}Br_x)₃ prior to and after dipping in the specific mixed solution with 8.25:1.75 mol ratio remain unchanged, confirming that MAPb(I_{1-x}Br_x)₃ before and after dipping remains stable (i.e. x = n). According to the above-mentioned similar procedures, the photocatalytic reaction solutions of MAPb(I_{1-x}Br_x)₃ (x = 0.05, 0.15, 0.20) are determined in sequence. As a result, a stability map of the MAPb(I_{1-x}Br_x)₃ in different mixed solutions is constructed (Fig. 4). The specific HI/HBr mixed solution that can remain MAPb(I_{1-x}Br_x)₃ before and after dipping stable are selected as photocatalytic reaction medium for H₂ evolution.

3.3. Photocatalytic HER activities

We evaluated the photocatalytic HER using a series of MAPb(I_{1-x}Br_x)₃ precipitates in the specific HI/HBr mixed solution under visible light ($\lambda \geq 420$ nm) irradiating (Fig. 5a). Obviously, MAPbI₃ exhibits a very low photocatalytic HER rate of 37 μmol h⁻¹ g⁻¹. After introducing Br anion into MAPbI₃, the photocatalytic HER activity of MAPb(I_{1-x}Br_x)₃ (x = 0.05, 0.10, 0.15 and 0.20) increases markedly. Particularly, the optimal MAPb(I_{1-x}Br_x)₃ (x = 0.10) shows a maximum photocatalytic HER rate of 1471 μmol h⁻¹ g⁻¹, which is approximately 40-fold higher than MAPbI₃, also superior to other commonly-used photocatalysts i.e. g-C₃N₄ and TiO₂ (Table S1). Cycling assay result of

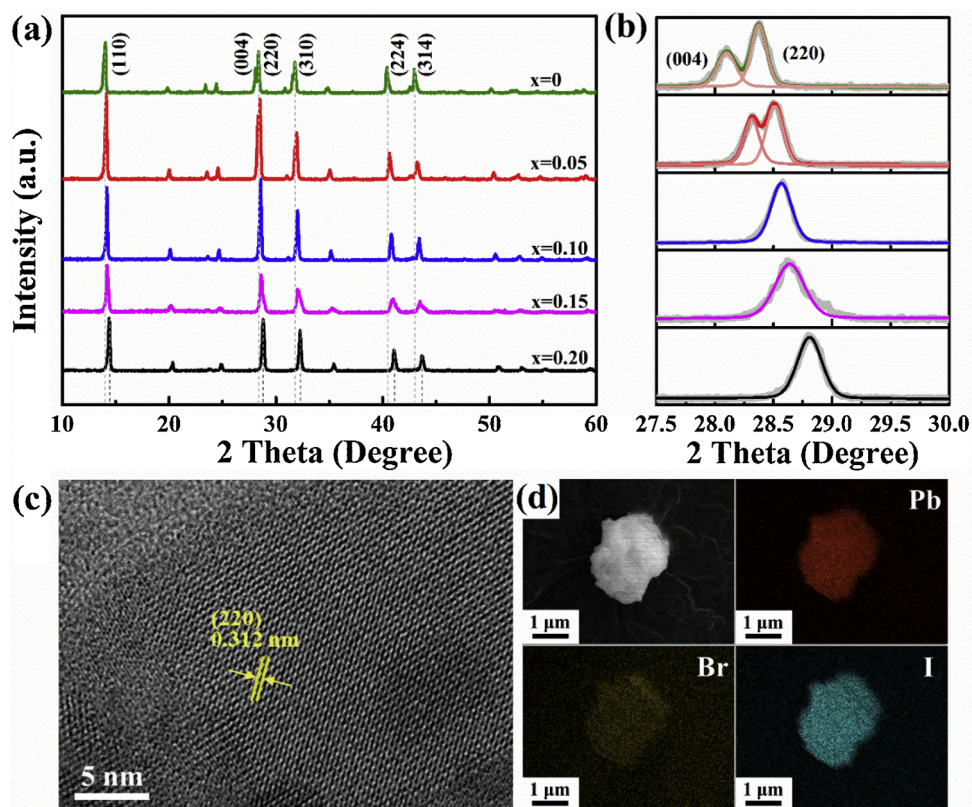


Fig. 2. (a) XRD patterns of the MAPb(I_{1-x}Br_x)₃ (x = 0–0.20) crystals. (b) The magnified XRD patterns in the region of the (004) and (220) peaks. (c) HR-TEM image and (d) SEM image and EDS mapping of MAPb(I_{1-x}Br_x)₃ (x = 0.10) crystal.

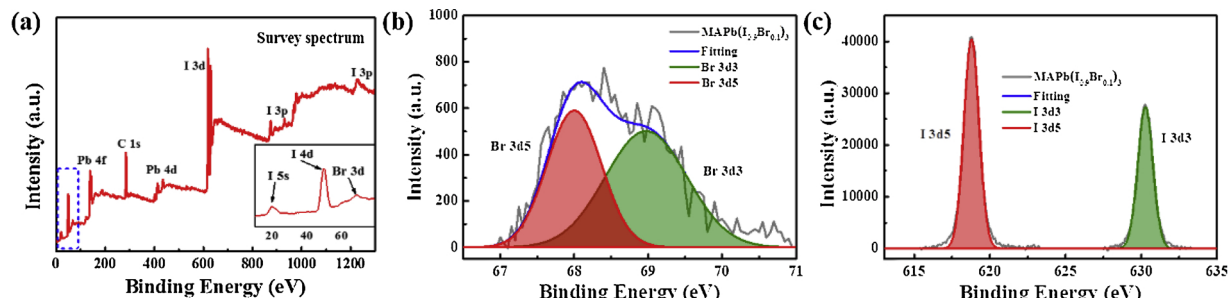


Fig. 3. (a) XPS survey spectrum and high-resolution (b) Br 3d and (c) I 3d spectra of MAPb(I_{1-x}Br_x)₃ (x = 0.10) crystal. Inset: the magnified region of the rectangle area.

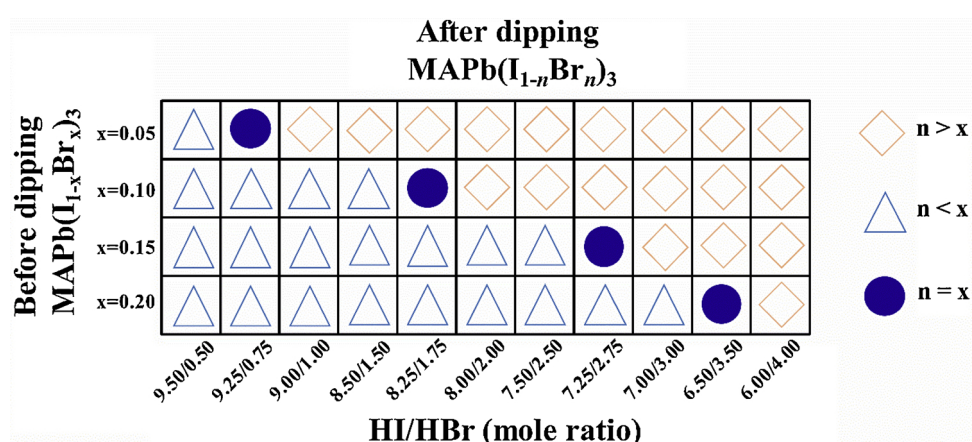


Fig. 4. Constructed stability map as the function of the HI/HBr ratio in the mixed solution. MAPb(I_{1-x}Br_x)₃ is the precipitated powder before dipping in HI/HBr mixed solution, while MAPb(I_{1-n}Br_n)₃ is the precipitated powder after that.

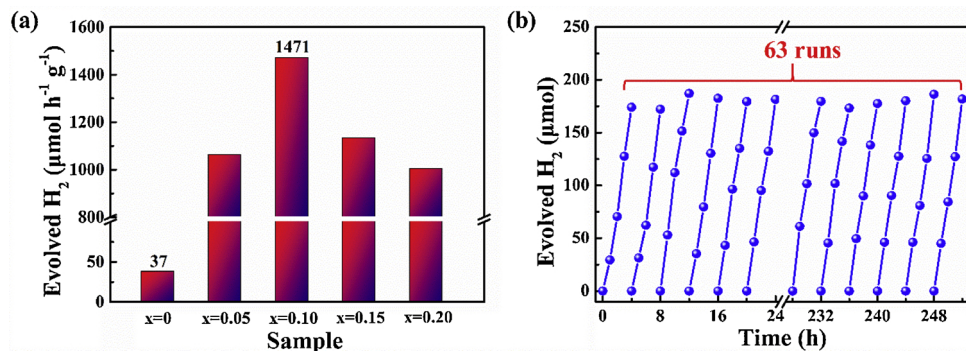


Fig. 5. (a) Photocatalytic H₂ evolution rate of MAPb(I_{1-x}Br_x)₃ (x = 0–0.20) crystals in saturated HI/HBr solution. (b) Recycle of H₂ evolution over the MAPb(I_{1-x}Br_x)₃ (x = 0.10) crystal after 252 h (i.e. 63 runs).

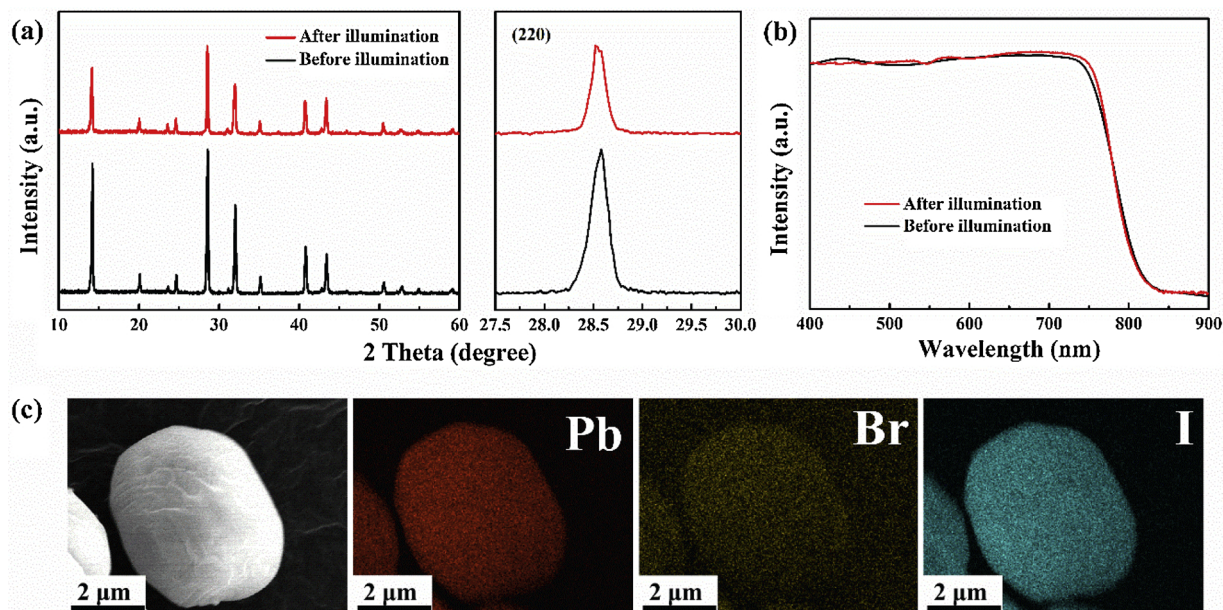


Fig. 6. (a) XRD patterns and (b) UV-vis light absorption spectra of as-prepared MAPb(I_{1-x}Br_x)₃ (x = 0.10) before and after being used for 252 h of photocatalytic H₂ evolution. (c) SEM image and EDS mapping of MAPb(I_{1-x}Br_x)₃ (x = 0.10) after being used for 252 h of photocatalytic H₂ evolution.

MAPb(I_{1-x}Br_x)₃ (x = 0.10) in Fig. 5b shows the excellent photostability and HER activity during 252 h (i.e., 63 cycles) under visible light irradiating. Furthermore, the structure and morphology of MAPb(I_{1-x}Br_x)₃ (x = 0.10) after photocatalytic reaction was carried out by means of a series of characterizations including XRD, UV-vis, and EDS mapping, as shown in Fig. 6a–c. All results show that no changes in phase/structure/composition of MAPb(I_{1-x}Br_x)₃ occur after 252 h of H₂ evolution, indicating the high stability of catalyst in aqueous HI/HBr mixed solution. The solar HI splitting efficiency of MAPb(I_{1-x}Br_x)₃ (x = 0.10) is calculated to 1.42% under visible light irradiation ($\lambda \geq 420$ nm) (Fig. S2; Experimental section), and the comparative data with other groups are also listed in Table S1.

3.4. Origin and analysis of the enhanced performance

To get insight into the catalytic mechanism, spectroscopic and photoelectrochemical studies were conducted [37]. The light absorption capability of MAPb(I_{1-x}Br_x)₃ was investigated by the UV-visible absorption spectra (Fig. S3a). With the increase of Br content from 0 to 0.20, all samples still exhibit strong absorption in whole visible light region. Meanwhile, the onset absorption band of MAPb(I_{1-x}Br_x)₃ shows a slight hypsochromic shift from 848 to 809 nm, which ascribes to the variation of band gap (E_g) of samples [38]. The corresponding E_g values are estimated using Kubelk-Munk method (Fig. S3b) [39]. The E_g values

of MAPb(I_{1-x}Br_x)₃ (x = 0–0.20) gradual enlarge with the increase of x, due to the hybridization of the Br (4p) orbitals with the I (5p) and Pb (6s) orbitals as well as a simultaneous structural transition in the MAPb(I_{1-x}Br_x)₃ compounds [40].

The photo-excited electron-hole separation and charge transfer can be investigated by a series of characterization techniques, e.g., steady-state PL spectra, transient-state PL spectra, transient photocurrent responses and EIS spectra. Fig. 7a shows the PL spectra of MAPb(I_{1-x}Br_x)₃ samples. One can observe that the emission peak positions of MAPb(I_{1-x}Br_x)₃ (x = 0–0.20) gradually shift from 800 to 754 nm with the increase of x from 0 to 0.20, consistent with their bandgap variations. Furthermore, the PL intensity first increases and then decreases as Br content increases from 0 to 0.20. An increase in the PL peak intensity might be attributed to the suppression of the non-radiative recombination of excitons. Such the increase of PL intensity caused by non-radiative recombination of excitons indeed has been reported in the domain of photovoltaic devices mediated by MAPbI₃/MAPbI_{3-x}Br_x materials [26,41]. Excessive Br (x > 0.10) facilitates the formation of trap states in the perovskite and gives rise to an increase of trap-induced non-radiative recombination, finally leading to a decrease in PL peak intensity [42,43]. In order to further gain insight into the decay behavior of photogenerated carriers in the samples, we also perform time-resolved PL spectra measurements and the corresponding results are shown in Fig. 7b and Table S2. According to the literature [43], the

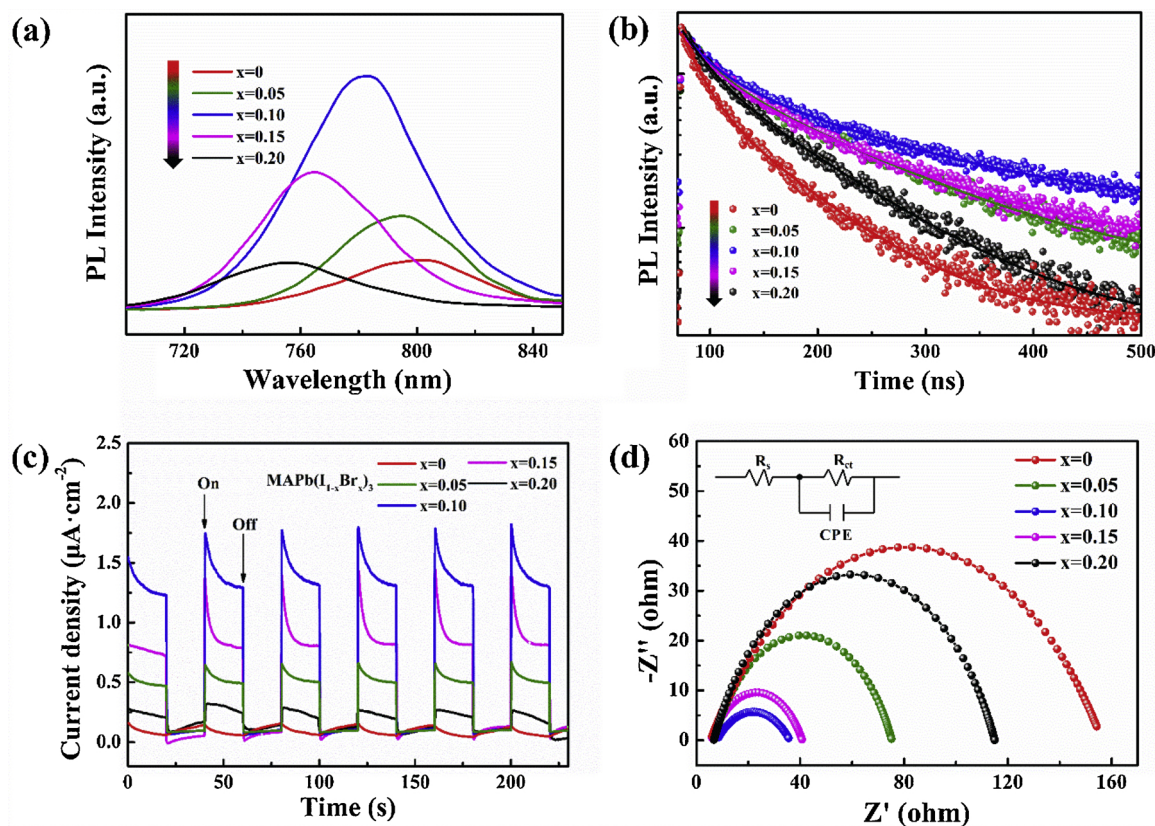


Fig. 7. (a) PL spectra and (b) time-resolved PL spectra of MAPb(I_{1-x}Br_x)₃ ($x = 0\text{--}0.20$) crystals. Visible light ($\lambda \geq 420\text{ nm}$) induced (c) transient photocurrent responses and (d) EIS plots of MAPb(I_{1-x}Br_x)₃ ($x = 0\text{--}0.20$) crystals in saturated HI/HBr solution.

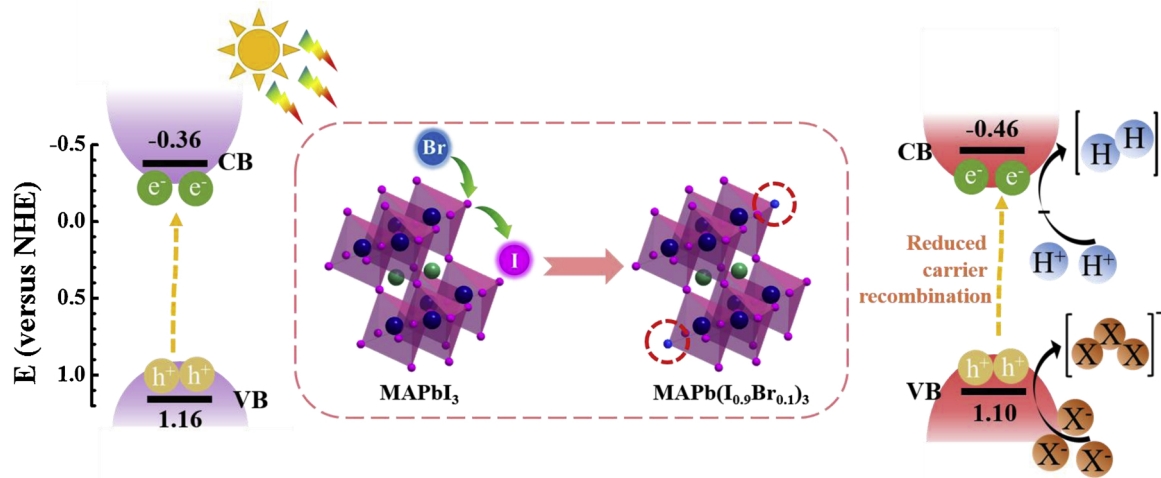
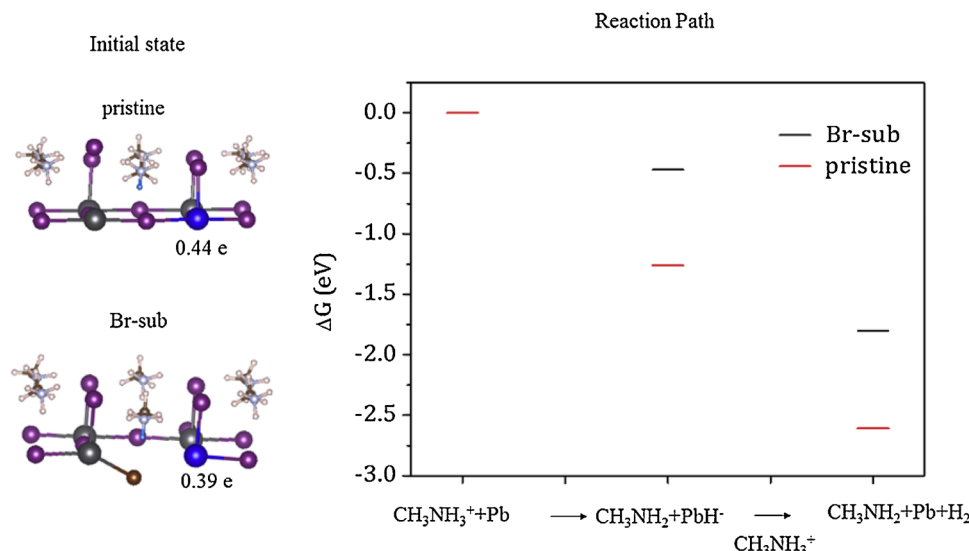


Fig. 8. Schematic band diagram of the MAPbI₃ and MAPb(I_{1-x}Br_x)₃ ($x = 0.10$) crystal for the HI splitting photocatalytic reaction.

average PL lifetime constants τ_{avg} are calculated and the MAPb(I_{1-x}Br_x)₃ ($x = 0.10$) sample reaches the maximum τ_{avg} value of 134.06 ns, approximately 2 times longer than 69.43 ns of MAPbI₃. The longer τ_{avg} indicates the long-lived photogenerated electrons, representing a higher probability of their involvement in the photocatalytic reaction before recombination, and resulting in enhanced HER activity [44,45]. Additionally, as compared to MAPbI₃, all the Br-incorporated samples exhibit a noticeable current increase in photocurrent responses upon visible light irradiation ($\lambda \geq 420\text{ nm}$), followed by a quick reverse back to the original state upon removal of the light source (Fig. 7c). This further indicates the added Br facilitates efficient separation and migration of photo-induced charge carriers in perovskite

photocatalyst [46]. The EIS also be measured to evaluate the charge transfer within photocatalysts. The radius of the arc in the EIS spectra reflects the interface layer resistance occurring at the electrode surface, and thus are fitted using a Randles equivalent circuit (inset in Fig. 7d). As shown in Fig. 7d, MAPb(I_{1-x}Br_x)₃ ($x = 0.10$) exhibits a smallest semicircle among all samples, implying the lowest charge transfer resistance and excellent carrier transport [47,48].

Since Br doping is observed to influence the sunlight absorption as well as the photocatalytic H₂ production (Fig. S3a and Fig. 5a), the energy band position of Br-doped perovskite that largely determines reduction capability of electrons should be evaluated. Herein, the E_g values of MAPbI₃ and MAPb(I_{1-x}Br_x)₃ ($x = 0.10$) are respectively



estimated to be 1.52 eV and 1.56 eV by analyzing the UV-vis light absorption spectra (Fig. S3b). The valence band positions (E_{VB}) measured from valence band XPS spectra (Fig. S4), are estimated to be at 1.16 eV for MAPbI_3 and 1.10 eV for $\text{MAPb}(\text{I}_{1-x}\text{Br}_x)_3$ ($x = 0.10$), respectively. As such, the conduction band potential (E_{CB}) of samples are obtained according to the common equation [49], $E_{CB} = E_{VB} - E_g$, namely, -0.36 eV for MAPbI_3 and -0.46 eV $\text{MAPb}(\text{I}_{1-x}\text{Br}_x)_3$ ($x = 0.10$) vs. NHE. Apparently, the E_{CB} of $\text{MAPb}(\text{I}_{1-x}\text{Br}_x)_3$ ($x = 0.10$) is more negative relative to MAPbI_3 . The more negative potential of CB could enhance the reduction capability of electrons, which is beneficial for the facilitating of HER [50]. Hence, we may conclude that Br doping can significantly tune the band structure of perovskite and negative shift the potential of CB, which can enhance the HER performance. The photocatalytic HER process of $\text{MAPb}(\text{I}_{1-x}\text{Br}_x)_3$ under visible light irradiation is schematically displayed in Fig. 8.

To deeply understand Br effects on enhancement in the photocatalytic HER process, density functional theory calculations were carried out. We focus mainly on Pb-activated amine-assisted catalytic process [51]. In the pristine (010) perovskite surface, the I-Pb bonds in the linear Pb-I-Pb linkage are 3.23 \AA and 3.19 \AA . After Br-substitution, the Pb-Br-Pb linkage breaks and becomes non-linear. The Br-Pb bonds are 3.15 \AA and 3.92 \AA . Thus, one of the Pb has lower coordination number and forms a defect site (blue ball in the Fig. 9), which is expected to cause the main change in the photocatalytic HER process. There are two steps in Pb-activated amine-assisted photocatalytic evolution reaction process. In the first step, an H from MA^+ is transferred to Pb, forming PbH^- . In the second step, the H of a MA^+ bonds with the H of PbH^- to form H_2 . For the first step, the H-Pb absorption energy with Br-substitution (-0.48 eV) is lower than that without Br-substitution (-1.27 eV). In the second step, the H_2 formation energies are similar with Br-substitution (-1.35 eV) and without Br-substitution (-1.36 eV). The lower H-Pb absorption energy indicates that it is easier to transfer an H from MA^+ to the Pb atom and eventually enhance the HER rate. Such an enhancement can be ascribed to two main reasons: 1) due to the smaller atomic radius of Br (0.196 nm) compared with I (0.220 nm), the Pb at the defect site (highlighted with blue in the Fig. 9), is exposed to amine cations in Br-incorporated perovskite, facilitating the transfer of H; 2) at the defected sites, the Pb is less positively charged (0.44 e in pristine, 0.39 e in Br-substituted), which makes the Pb-H energy in Br-incorporated perovskite weaker, facilitating the formation of H_2 .

4. Conclusions

In conclusion, $\text{MAPb}(\text{I}_{1-x}\text{Br}_x)_3$ perovskites fabricated by varying

the halide composition of the perovskite precursor solution have been successfully employed as photocatalysts for HER in aqueous HI/HBr solution with no Pt as a cocatalyst. An optimized $\text{MAPb}(\text{I}_{1-x}\text{Br}_x)_3$ ($x = 0.10$) photocatalyst shows a superb HER rate of $1471\text{ }\mu\text{mol h}^{-1}\text{ g}^{-1}$ under visible light ($\lambda \geq 420$ nm) illumination, which is ~ 40 times higher than that of pure MAPbI_3 . This dual-halide perovskite also is rather stable showing almost no decrease in the photocatalytic recycling process. The solar HI splitting efficiency of $\text{MAPb}(\text{I}_{1-x}\text{Br}_x)_3$ ($x = 0.10$) is determined as 1.42% . The photocatalytic HER enhancement is mainly attributable to the Pb at the defect site exposed to amine cations and a lower Pb-H energy in the Br-incorporated perovskite. This is the first exploration on one-pot-synthesized stable hybrid perovskite $\text{MAPb}(\text{I}_{1-x}\text{Br}_x)_3$ photocatalyst for H_2 evolution. This work provides a valuable and practical guide to fabricate hybrid organic-inorganic perovskite for high-performance HI splitting.

Acknowledgement

This work was supported financially by National Natural Science Foundation of China (Nos. 21476019, 21676017).

Appendix A. Supplementary data

Supplementary material related to this article can be found, in the online version, at doi:<https://doi.org/10.1016/j.apcatb.2019.04.050>.

References

- [1] H. Chen, F. Ye, W. Tang, J. He, M. Yin, Y. Wang, F. Xie, E. Bi, X. Yang, M. Grätzel, *Nature* 550 (2017) 92.
- [2] W.S. Yang, B.W. Park, E.H. Jung, N.J. Jeon, Y.C. Kim, D.U. Lee, S.S. Shin, J. Seo, E.K. Kim, J.H. Noh, *Science* 356 (2017) 1376–1379.
- [3] A. Rajagopal, Z. Yang, S.B. Jo, I.L. Braly, P.W. Liang, H.W. Hillhouse, A.K. Jen, *Adv. Mater.* 29 (2017) 1702140.
- [4] V. Jella, S. Ippili, J.-H. Eom, J. Choi, S.-G. Yoon, *Nano Energy* 53 (2018) 46–56.
- [5] J. Li, T. Jiu, C. Duan, Y. Wang, H. Zhang, H. Jian, Y. Zhao, N. Wang, C. Huang, Y. Li, *Nano Energy* 46 (2018) 331–337.
- [6] F.L. Meng, J.J. Wu, E.F. Zhao, Y.Z. Zheng, M.L. Huang, L.M. Dai, X. Tao, J.F. Chen, *Nanoscale* 9 (2017) 18535–18545.
- [7] X. Lai, X. Li, X. Lv, Y.-Z. Zheng, F. Meng, X. Tao, *J. Power Sources* 372 (2017) 125–133.
- [8] Y. Zhang, Z. Zhou, F. Ji, Z. Li, G. Cui, P. Gao, E. Oveisi, M.K. Nazeeruddin, S. Pang, *Adv. Mater.* 30 (2018) e1707143.
- [9] S. Park, W.J. Chang, C.W. Lee, S. Park, H.-Y. Ahn, K.T. Nam, *Nat. Energy* 2 (2016) 16185.
- [10] P. Da, M. Cha, L. Sun, Y. Wu, Z.S. Wang, G. Zheng, *Nano Lett.* 15 (2015) 3452–3457.
- [11] M.T. Hoang, N.D. Pham, J.H. Han, J.M. Gardner, I. Oh, *ACS Appl. Mater. Interfaces* 8 (2016) 11904–11909.

[12] Z. Xiao, R.A. Kerner, L. Zhao, N.L. Tran, K.M. Lee, T.W. Koh, G.D. Scholes, B.P. Rand, *Nat. Photonics* 11 (2017) 108–115.

[13] L. Meng, E.P. Yao, Z. Hong, H. Chen, P. Sun, Z. Yang, G. Li, Y. Yang, *Adv. Mater.* 29 (2017) 1603826.

[14] Q. Zhang, R. Su, W. Du, X. Liu, L. Zhao, S.T. Ha, Q. Xiong, *Small Methods* 1 (2017) 1700163.

[15] Y. Fu, H. Zhu, A.W. Schrader, D. Liang, Q. Ding, P. Joshi, L. Hwang, X. Zhu, S. Jin, *Nano Lett.* 16 (2016) 1000–1008.

[16] K.C. Kwon, K. Hong, Q. Van Le, S.Y. Lee, J. Choi, K.B. Kim, S.Y. Kim, H.W. Jang, *Adv. Funct. Mater.* 26 (2016) 4213–4222.

[17] J. Newson, A. Riddiford, *J. Electrochem. Soc.* 108 (1961) 699–706.

[18] C. Levy-Clement, A. Heller, W. Bonner, B. Parkinson, *J. Electrochem. Soc.* 129 (1982) 1701–1705.

[19] N.D. McDaniel, S. Bernhard, *Dalton Trans.* 39 (2010) 10021–10030.

[20] G.R. Taylor, M. Butler, *J. Hyg.* 89 (1982) 321–328.

[21] X. Wang, H. Wang, H. Zhang, W. Yu, X. Wang, Y. Zhao, X. Zong, C. Li, *ACS Energy Lett.* 3 (2018) 1159–1164.

[22] Y. Wu, P. Wang, X. Zhu, Q. Zhang, Z. Wang, Y. Liu, G. Zou, Y. Dai, M.H. Whangbo, B. Huang, *Adv. Mater.* 30 (2018) 1704342.

[23] G. Gordillo, C.A. Otálora, M.A. Reinoso, *J. Mater. Sci.: Mater. Electron.* 29 (2017) 4276–4284.

[24] Y. Wu, P. Wang, Z. Guan, J. Liu, Z. Wang, Z. Zheng, S. Jin, Y. Dai, M.-H. Whangbo, B. Huang, *ACS Catal.* 8 (2018) 10349–10357.

[25] P.-W. Liang, C.-C. Chueh, X.-K. Xin, F. Zuo, S.T. Williams, C.-Y. Liao, A.K.Y. Jen, *Adv. Energy Mater.* 5 (2015) 1400960.

[26] W. Zhu, C. Bao, F. Li, T. Yu, H. Gao, Y. Yi, J. Yang, G. Fu, X. Zhou, Z. Zou, *Nano Energy* 19 (2016) 17–26.

[27] A. Sadhanala, F. Deschler, T.H. Thomas, S.E. Dutton, K.C. Goedel, F.C. Hanusch, M.L. Lai, U. Steiner, T. Bein, P. Docampo, *J. Phys. Chem. Lett.* 5 (2014) 2501–2505.

[28] S. de Gironcoli, *Phys. Rev. B* 51 (1995) 6773–6776.

[29] C.-L. Fu, K.-M. Ho, *Phys. Rev. B* 28 (1983) 5480–5486.

[30] M. Gajdoš, K. Hummer, G. Kresse, J. Furthmüller, F. Bechstedt, *Phys. Rev. B* 73 (2006) 045112.

[31] M. Hutchinson, M. Widom, *Comput. Phys. Commun.* 183 (2012) 1422–1426.

[32] P.E. Blöchl, *Phys. Rev. B* 50 (1994) 17953–17979.

[33] S. Grimme, J. Antony, S. Ehrlich, H. Krieg, *J. Chem. Phys.* 132 (2010) 154104.

[34] J.H. Noh, S.H. Im, J.H. Heo, T.N. Mandal, S.I. Seok, *Nano Lett.* 13 (2013) 1764–1769.

[35] V. Malgras, J. Henzie, T. Takei, Y. Yamauchi, *Chem. Commun.* 53 (2017) 2359–2362.

[36] C.M. Sutter-Fella, Y. Li, M. Amani, J.W. Ager III, F.M. Toma, E. Yablonovitch, I.D. Sharp, A. Javey, *Nano Lett.* 16 (2015) 800–806.

[37] J. Wu, N. Li, X.-H. Zhang, H.-B. Fang, Y.-Z. Zheng, X. Tao, *Appl. Catal. B: Environ.* 226 (2018) 61–70.

[38] Y. Zhang, Y. Liu, Y. Li, Z. Yang, S. Liu, J. Mater. Chem. C 4 (2016) 9172–9178.

[39] M. Wu, J. Zhang, B.-b. He, H.-w. Wang, R. Wang, Y.-s. Gong, *Appl. Catal. B: Environ.* 241 (2019) 159–166.

[40] J. Qiu, Y. Qiu, K. Yan, M. Zhong, C. Mu, H. Yan, S. Yang, *Nanoscale* 5 (2013) 3245–3248.

[41] F.-L. Meng, J.-J. Wu, E.-F. Zhao, Y.-Z. Zheng, M.-L. Huang, L.-M. Dai, X. Tao, J.-F. Chen, *Nanoscale* 9 (2017) 18535–18545.

[42] T. Zhang, M. Long, K. Yan, X. Zeng, F. Zhou, Z. Chen, X. Wan, K. Chen, P. Liu, F. Li, *ACS Appl. Mater. Interfaces* 8 (2016) 32366–32375.

[43] F. Zhang, B. Yang, X. Mao, R. Yang, L. Jiang, Y. Li, J. Xiong, Y. Yang, R. He, W. Deng, K. Han, *ACS Appl. Mater. Interfaces* 9 (2017) 14827–14832.

[44] Y. Li, R. Jin, Y. Xing, J. Li, S. Song, X. Liu, M. Li, R. Jin, *Adv. Energy Mater.* 6 (2016) 1601273.

[45] H.-F. Ye, R. Shi, X. Yang, W.-F. Fu, Y. Chen, *Appl. Catal. B: Environ.* 233 (2018) 70–79.

[46] H.-B. Fang, X.-H. Zhang, J. Wu, N. Li, Y.-Z. Zheng, X. Tao, *Appl. Catal. B: Environ.* 225 (2018) 397–405.

[47] W. Li, Y. Liu, M. Wu, X. Feng, S.A.T. Redfern, Y. Shang, X. Yong, T. Feng, K. Wu, Z. Liu, B. Li, Z. Chen, J.S. Tse, S. Lu, B. Yang, *Adv. Mater.* 30 (2018) e1800676.

[48] Y.-S. Chang, M. Choi, M. Baek, P.-Y. Hsieh, K. Yong, Y.-J. Hsu, *Appl. Catal. B: Environ.* 225 (2018) 379–385.

[49] Y. Deng, L. Tang, G. Zeng, Z. Zhu, M. Yan, Y. Zhou, J. Wang, Y. Liu, J. Wang, *Appl. Catal. B: Environ.* 203 (2017) 343–354.

[50] J. Guo, X. Liao, M.-H. Lee, G. Hyett, C.-C. Huang, D.W. Hewak, S. Mailis, W. Zhou, Z. Jiang, *Appl. Catal. B: Environ.* 243 (2019) 502–512.

[51] L. Wang, H. Xiao, T. Cheng, Y. Li, W.A. Goddard 3rd, J. Am. Chem. Soc. 140 (2018) 1994–1997.